NASA/TM–20210022123

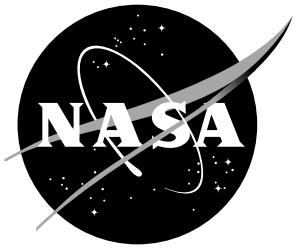

Identification of Best Practices for Predicting Inlet Performance Using FUN3D Part 1: Isolated S-Duct

Jan-Reneé Carlson and Michael D. Bozeman, Jr.
Langley Research Center, Hampton, Virginia

March 2022

NASA STI Program Report Series

Since its founding, NASA has been dedicated to the advancement of aeronautics and space science. The NASA scientific and technical information (STI) program plays a key part in helping NASA maintain this important role.

The NASA STI program operates under the auspices of the Agency Chief Information Officer. It collects, organizes, provides for archiving, and disseminates NASA's STI. The NASA STI program provides access to the NTRS Registered and its public interface, the NASA Technical Reports Server, thus providing one of the largest collections of aeronautical and space science STI in the world. Results are published in both non-NASA channels and by NASA in the NASA STI Report Series, which includes the following report types:

- TECHNICAL PUBLICATION. Reports of completed research or a major significant phase of research that present the results of NASA Programs and include extensive data or theoretical analysis. Includes compilations of significant scientific and technical data and information deemed to be of continuing reference value. NASA counterpart of peer-reviewed formal professional papers but has less stringent limitations on manuscript length and extent of graphic presentations.

- TECHNICAL MEMORANDUM. Scientific and technical findings that are preliminary or of specialized interest, e.g., quick release reports, working papers, and bibliographies that contain minimal annotation. Does not contain extensive analysis.

- CONTRACTOR REPORT. Scientific and technical findings by NASA-sponsored contractors and grantees.

- CONFERENCE PUBLICATION. Collected papers from scientific and technical conferences, symposia, seminars, or other meetings sponsored or co-sponsored by NASA.

- SPECIAL PUBLICATION. Scientific, technical, or historical information from NASA programs, projects, and missions, often concerned with subjects having substantial public interest.

- TECHNICAL TRANSLATION. English-language translations of foreign scientific and technical material pertinent to NASA's mission.

Specialized services also include organizing and publishing research results, distributing specialized research announcements and feeds, providing information desk and personal search support, and enabling data exchange services.

For more information about the NASA STI program, see the following:

- Access the NASA STI program home page at http://www.sti.nasa.gov

- Help desk contact information:

https://www.sti.nasa.gov/sti-contact-form/
and select the "General" help request type.

NASA/TM–20210022123

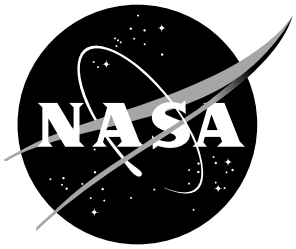

Identification of Best Practices for Predicting Inlet Performance Using FUN3D Part 1: Isolated S-Duct

Jan-Reneé Carlson and Michael D. Bozeman, Jr.
Langley Research Center, Hampton, Virginia

National Aeronautics and
Space Administration

Langley Research Center
Hampton, Virginia 23681-2199

March 2022

Available from:

NASA STI Program / Mail Stop 148
NASA Langley Research Center
Hampton, VA 23681-2199
Fax: 757-864-6500

Abstract

Variations in numerical model and location of the outflow boundary of a generic S-duct inlet test configuration were investigated. Outflow models were a choked convergent nozzle, back pressure using the averaged Mach number at the aerodynamic interface plane (AIP), mass flow rate, and fixed static pressure, placed at several streamwise locations downstream of the AIP. Iterative convergence was important to predict the symmetric vortex pair passing through the AIP. Distortion and mass flow rate varied slightly depending on model. A hysteresis in the predicted inlet distortion levels was observed with static pressure outflow boundary value sweeps. Moving the outflow boundary location closer to the AIP varied the shape and degree of hysteresis with no discernible consistent trend.

1 Introduction

As part of the NASA Civilian Supersonic Transport project, an effort was launched to revisit the computational fluid dynamic (CFD) modeling of inlet and nozzle geometries and flows. This study surveys several methods for modeling the flow in a curved S-duct and the influence that geometry and boundary condition have on the mass flow and distortion at the aerodynamic interface plane (AIP). The inflow boundary condition is typically less of an issue since the reference Mach number determines the total conditions. The more difficult tasks are choosing the most appropriate boundary condition and value of boundary parameters to achieve the desired flow conditions at the inlet and the AIP. Four outflow boundary configurations are considered in this study: 1) A choked nozzle outflow configuration, 2) specifying the mass flow rate, 3) fixed static pressure, and 4) setting back-pressure to achieve a specific Mach number at the AIP. The location of the outflow boundary was varied from coincident with the AIP to 40 duct diameters downstream of the AIP.

The computational method and boundary conditions are discussed in Sec. 2, followed by a description of the problem setup, Sec. 3. Changes to the grid topology and the current boundary condition results are discussed in Sec. 4.

2 Computational Method

FUN3D is an unstructured three-dimensional, implicit, Navier-Stokes code. Roe's flux difference splitting [1] is used for the calculation of the inviscid terms. The method for calculation of the Jacobian was the flux function of van Leer [2]. Flux limiters were not used in any of the simulations. Other details regarding FUN3D can be found in the manual [3], as well as in the extensive bibliography that is accessible at the FUN3D Web site [4]. Solutions were computed using the Spalart-Allmaras (negative) turbulence model [5] with the rotational correction [6] and Quadratic Constitutive Relation (QCR) 2000 [7]. All simulations for this paper were run in the steady-state mode using local time stepping.

3 Problem Description

An isolated inlet test rig was modeled as an internal flow problem. Perspective and symmetry views of the baseline outflow location with a choked nozzle shown in Fig. 1. The computational models had an upstream low-speed plenum, inlet duct section upstream of the AIP, and downstream duct section followed by an outflow boundary configuration. The S-duct geometry shifted the plenum and inlet duct entrance center offset 3.5-inches from the AIP center

shown in Fig. 1a. The cross-section of the model was circular throughout the whole geometry to eliminate the upstream corner vortices that can occur when using a rectangular cross-section in the upstream plenum. The five positions of the outflow boundary are shown in Fig. 1b, though for this phase of the study, locating the outflow boundary at the AIP was eliminated as a choice. The radius of the upstream plenum was 15.0 inches (area of 706.9 square inches). The AIP was located at x = 0.0 with 10-inch spacing between each successive outflow boundary. The radius of the circular cross-section at the AIP was 3.75 inches (area of 44.2 square inches).

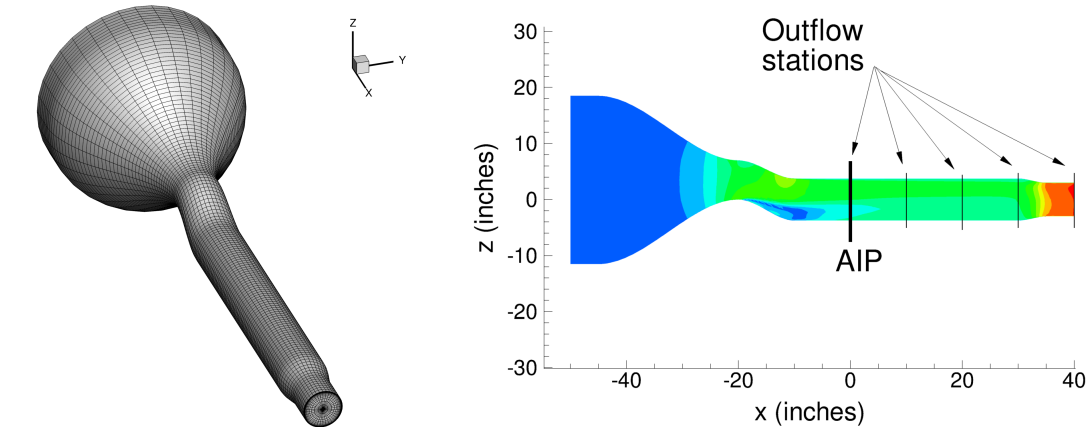

(a) Perspective view, coarse grid.

(b) Sketch of boundary condition stations.

Figure 1. Sketches of S-duct geometry, 3.5" offset.

3.1 Outflow Boundary Modeling

The typical boundary condition choices for modeling a purely internal flow is to specify the total conditions, pressure and temperature, at the inflow [8–10] and static pressure at the outflow. Often, the outflow static pressure level is not known a priori or is not a primary parameter of the simulation. Often, the problem is driven by a required mass flow rate or Mach number at some location in the flow. The desired result is still ultimately achieved by using a static pressure outflow boundary condition, via any number of different methodologies to determine exactly what the value needs to be. Four outflow modeling types were evaluated in this report and are described in the following subsections.

3.1.1 Choked nozzle

This outflow boundary configuration terminates the downstream constant area duct with a convergent cubic nozzle similar to the Boeing calibration nozzles discussed in Ref. [11]. The nozzle had a 5-inch long C1-continuous cubic

polynomial closure followed by a 5-inch constant area section to the nozzle exit. The radius of the circular cross-section of the downstream duct was 3.75 inches. The radius of the circular cross-section at the exit of the nozzle was 3.0 inches resulting in an exit area of 28.274 square inches. The total conditions at the inflow were a total pressure ratio of 2.0 and total temperature ratio of 1.22, which should ensure choked flow at the nozzle exit.

3.1.2 Mass flow rate specified at the outflow boundary

The mass flow boundary condition uses a PID-controller[1]to achieve the requested mass flow rate at the boundary. Further details concerning the PID-controller methodology can be found in Carlson [12]. At every iteration, the flow through the outflow boundary is integrated using the primal mesh. The result, processed by the PID controller, updates the back-pressure boundary condition to attain the requested mass flow rate.

3.1.3 Mach number (average) specified at the AIP

The fixed Mach number outflow boundary type is numerically inconsistent as an outflow boundary when abutting a viscous solid wall. The modeling is slightly modified, using an inviscid slip wall upstream of the outflow boundary mitigated this issue to some degree.

For the 4th AIAA Propulsion Aerodynamics Workshop (PAW04), Carter et al. [13] used the Proportional-Integer-Derivative (PID) controller developed by Carlson [12] to drive the outflow back-pressure simulations of an S-duct inlet configuration. For PAW04, the controller used the Mach number calculated from a 40-probe survey rake facsimile (the physical rake was not modeled) located at the AIP. Initially implemented by Endo [14] at the Glenn Research Center, the 40-probe rake concept was replaced by a control plane surface integration at the AIP for calculating the mass flow rate of the duct. Then, rather than specifying an average Mach number at the outflow boundary, the average Mach at the AIP is used as the control parameter. The PID-controller in FUN3D monitors the average Mach number at the AIP and drives the back-pressure to achieve the user requested condition at the AIP.

3.1.4 Fixed static pressure specified at the outflow boundary

The fourth outflow boundary type used in this study is the fixed static pressure ratio applied at the outflow boundary. Additional details on the implementation of boundary conditions in FUN3D can be found in Carlson [10].

[1]Proportional-Integral-Differential controller

4 Discussions

A short discussion of the grid topology, Sec. 4.1, is followed by results from the coarse and medium grid size runs in Secs. 4.2 and 4.3, respectively. Section 4.3.3 discusses the mass flow and distortion characteristics for each of the boundary output types and locations. Observations on the occurrence of multiple solutions using the mass flow rate and Mach controllers are discussed in Secs. 4.3.4, 4.3.5. The final section, Sec. 4.4, examines a hysteresis pattern in the prediction of distortion depending on the solution path.

4.1 Grid parameters.

The size of the grids used are listed in Table 4.1. All the grids were of structured hexahedral type that were converted into an unstructured form for use by FUN3D. A fine grid was generated for only the baseline configurations. Solutions were computed using the Spalart-Almaras (negative) turbulence model [5] with the rotational correction [6] and QCR [7]. All simulations for this paper were run in the steady-state mode.

Table 1. Grid sizing.

Grid	Outflow boundary streamwise location[1]				
	40.0	30.0	20.0	10.0	0.0
Coarse	153,027	136,371	229,725	103,059	86,403
Medium	1,209,797	1,077,669	945,541	813,413	681,285
Fine	9,622,655	—	—	—	—

[1] Location is in units of inches.

The cross-section of two axisymmetric grids are shown in Fig. 2. Typically, axisymmetric grids have been generated with a central pole region as shown in Fig. 2a. As explained in Nishikawa [15], there are issues with calculating accurate gradients on O-topology meshes that often occur with axisymmetric grids. The O-topology can result in a bias in the gradients around the pole when there are large number of coplanar nodes surrounding a central node on the centerline. The errors in the gradients are not overtly obvious with coarser meshes, but become increasingly worse as the mesh is refined. For this study, the central pole was replaced with an H-grid as shown in Fig. 2b.

4.2 Coarse Grid Solutions

Iterative convergence for the continuity and turbulence equations for solutions on the 3.5-inch offset duct geometries are shown in Fig. 3. Solution residuals

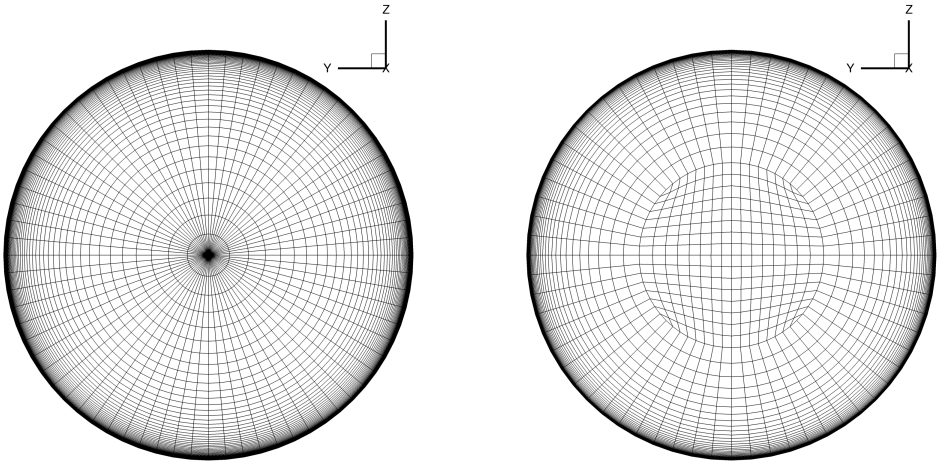

(a) Spoked grid topology, AIP. (b) H-grid core topology, AIP.

Figure 2. Comparison of grid topologies, medium grid density.

approached 'machine zero' for all four outflow boundary types. Similar solution residual trends occurred for all of the outflow boundary locations.

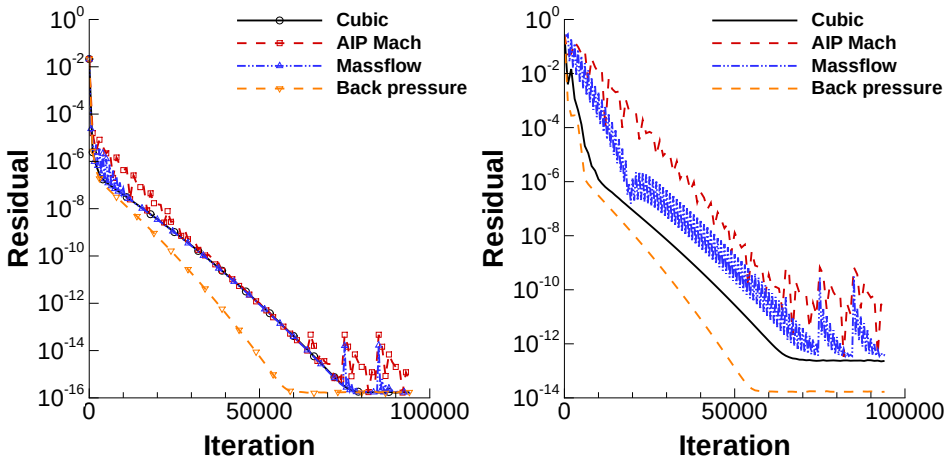

(a) Continuity equation. (b) Turbulence equation.

Figure 3. Variation of residuals with outflow boundary type, $x_{exit} = 40$ (baseline configuration).

Velocity contours for the choked nozzle outflow boundary coarse grid solutions are shown in Fig. 4. To more clearly see variations in the velocity contours in the AIP, the velocity scale has been magnified in Figs. 4b-4e and the three subsequent AIP flowfield figures, compared to the scale used for vertical centerplane contour plots. The separation bubble along the lower part of the duct does not appear to change much as the outflow boundary is shifted

forward, see Fig. 4a. The influence of nozzle contraction, however, does begin to alter the flowfield around the AIP. The most upstream position of the nozzle significantly alters the predicted velocities in that location. Streamwise velocity contours at the AIP for each outflow boundary location are plotted in Figs. 4b-4e. The predicted streamwise velocity at the AIP was mildly sensitive to the outflow boundary location with the most noticeable shift occurring with the x_{exit} = 10 location.[2] A single, asymmetric vortical feature passing through the AIP was predicted regardless of the location of the outflow boundary.

Velocity contours extracted from coarse grid solutions developed using the AIP Mach number controller are shown in Fig. 5. This sequence of outflow boundary location simulations appears to have two solution paths. The streamwise velocity contours in the vertical centerplane show no reversed flow upstream of the AIP for x_{exit} = 30 and 40 boundary outflow locations, see Fig. 5a, while the two outflow locations, x_{exit} = 10 and 20, show an extensive region of reverse flow in the lower portion of the S-curve. Additionally, the streamwise velocity field in the plane of the AIP, shown in Figs. 5b-5e, display more localized, bimodal contours associated with attached flow solution, as opposed to the larger, single-mode contours associated with the separated flow solution. Note that the single-mode phenomena was also observed for the choked nozzle outflow type solutions.

Velocity contours extracted from coarse grid solutions developed using the mass flow rate controller are shown in Fig. 6. All outflow boundary location simulations showed a region of separated flow upstream of the AIP, similar to the choked nozzle outflow type solutions. The streamwise velocity field in the plane of the AIP, shown in Figs. 6b-6e, exhibited the larger, single-mode contours associated with the separated flow solutions.

Velocity contours extracted from coarse grid solutions developed using the fixed static pressure outflow boundary are shown in Fig. 7. This sequence of outflow boundary location simulations also displays two solution paths. The streamwise velocity contours in the vertical centerplane show no reverse flow upstream of the AIP for x_{exit} = 30 and 40 boundary outflow locations, see Fig. 7a, while the outflow locations at x_{exit} = 10 and 20, again display a region of reverse flow. The streamwise velocity field in the plane of the AIP, as plotted in Figs. 7b-7e, has the same bimodal contours for outflow boundary locations of x_{exit} = 30 and 40, and the same larger, single-mode contours for outflow boundary locations of x_{exit} = 10 and 20.

[2] All locations and exit stations are in units of inches.

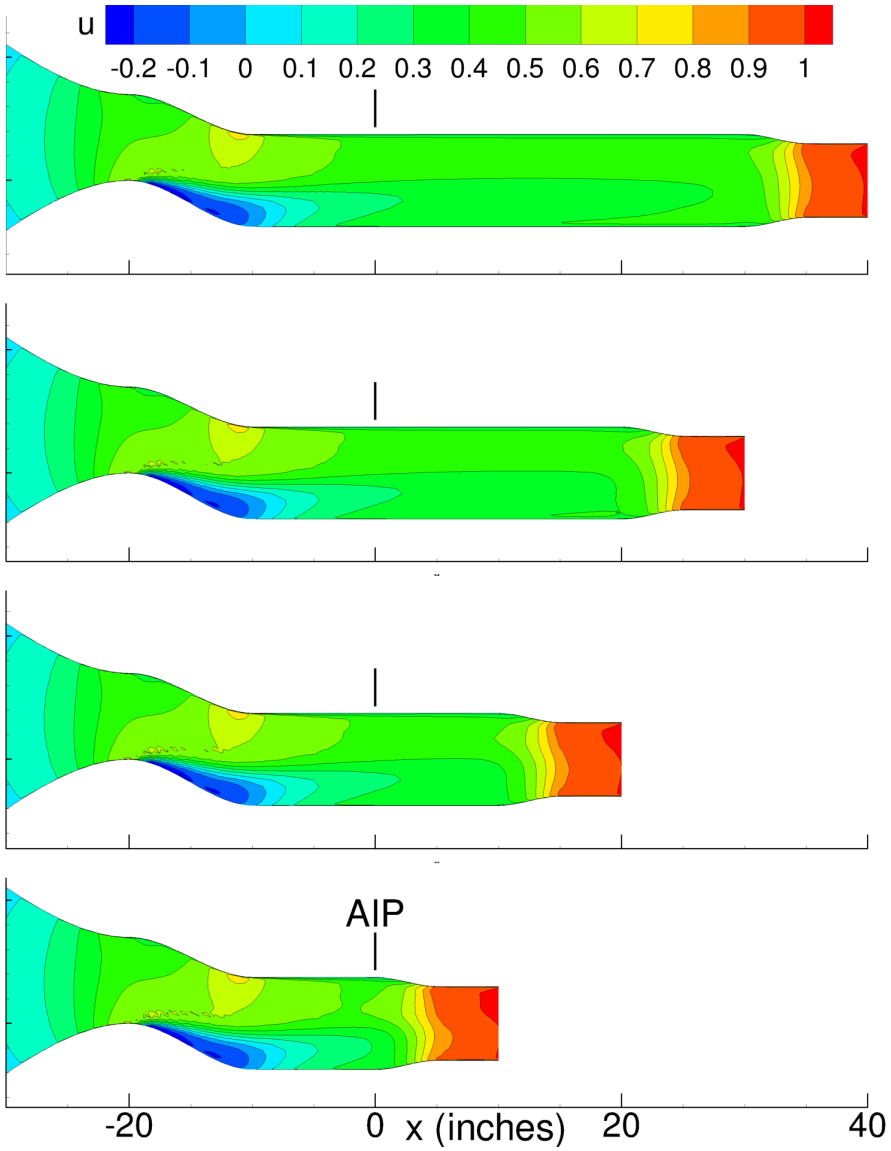

(a) Velocity contours, vertical centerplane.

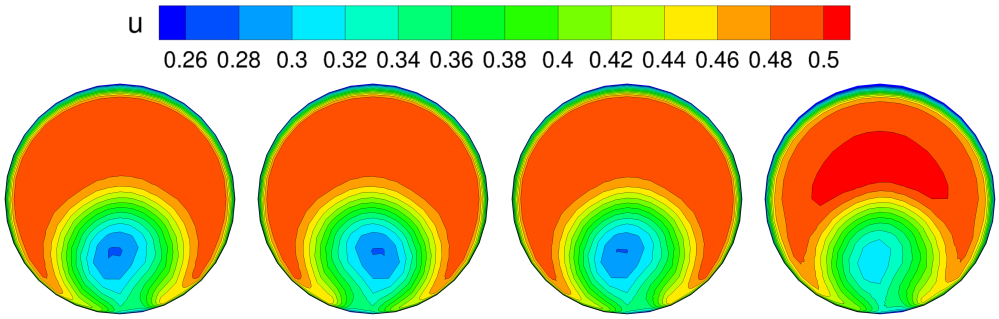

(b) AIP, $x_{exit} = 40$. (c) AIP, $x_{exit} = 30$. (d) AIP, $x_{exit} = 20$. (e) AIP, $x_{exit} = 10$.

Figure 4. Velocity contours, choked nozzle outflow type, coarse grid, velocity non-dimensionalized by the reference speed of sound.

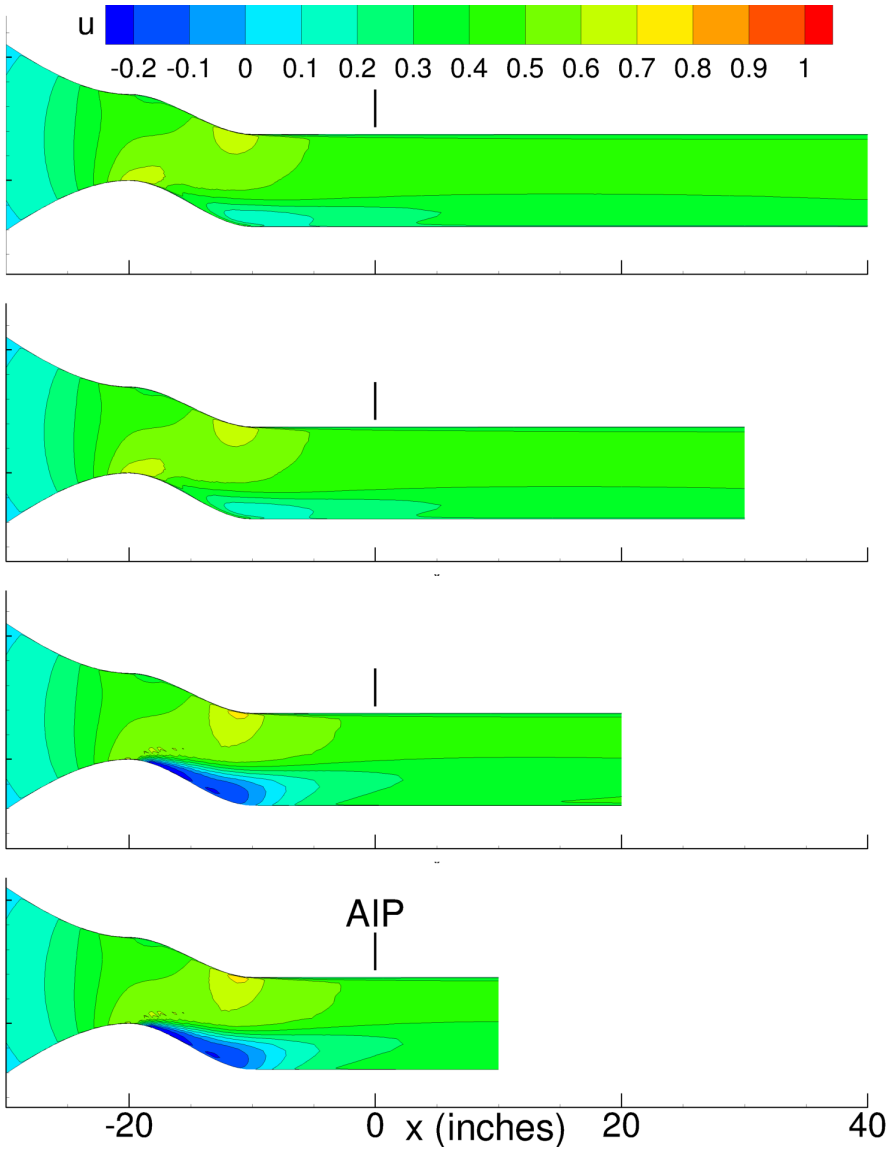

(a) Velocity contours, vertical centerplane.

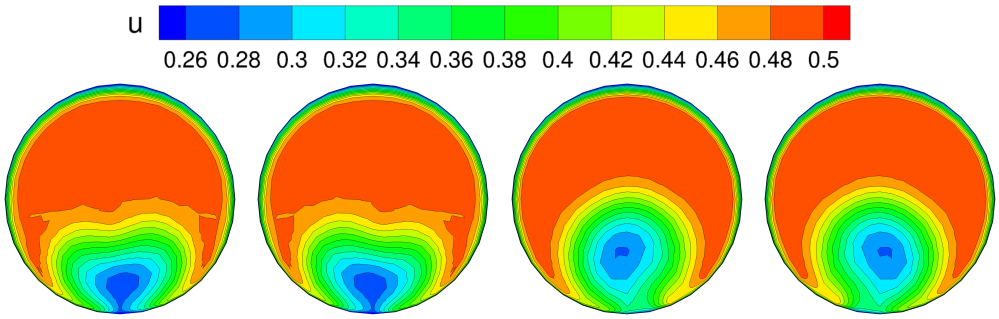

(b) AIP, $x_{exit} = 40$. (c) AIP, $x_{exit} = 30$. (d) AIP, $x_{exit} = 20$. (e) AIP, $x_{exit} = 10$.

Figure 5. Velocity contours, AIP Mach number controller outflow type, coarse grid, velocity non-dimensionalized by the reference speed of sound.

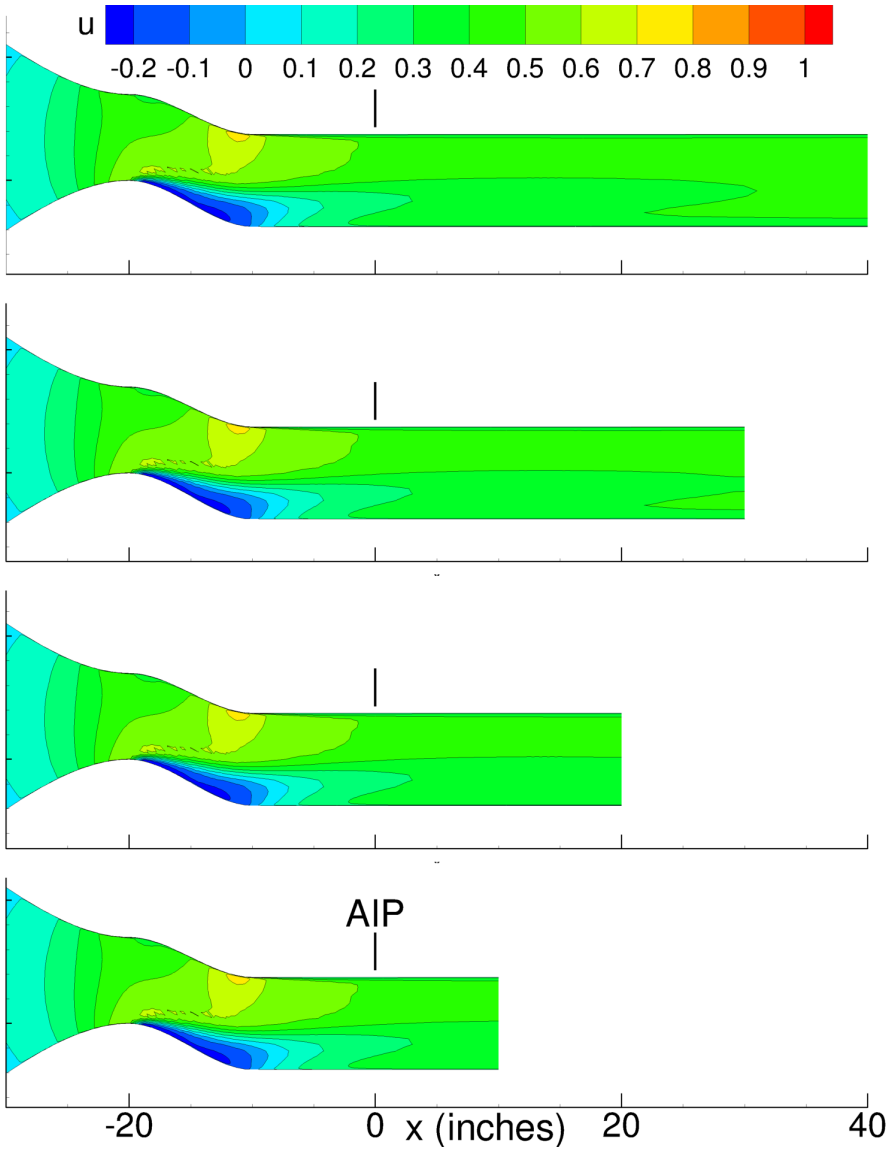

(a) Velocity contours, vertical centerplane.

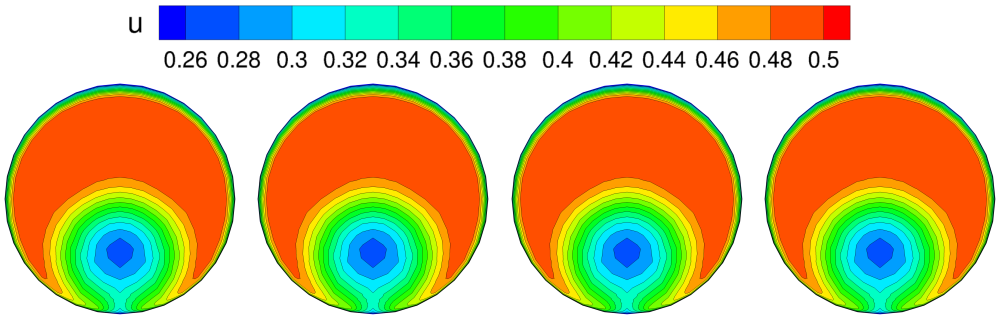

(b) AIP, $x_{exit} = 40$. (c) AIP, $x_{exit} = 30$. (d) AIP, $x_{exit} = 20$. (e) AIP, $x_{exit} = 10$.

Figure 6. Velocity contours, mass flow rate controller outflow type, coarse grid, velocity non-dimensionalized by the reference speed of sound.

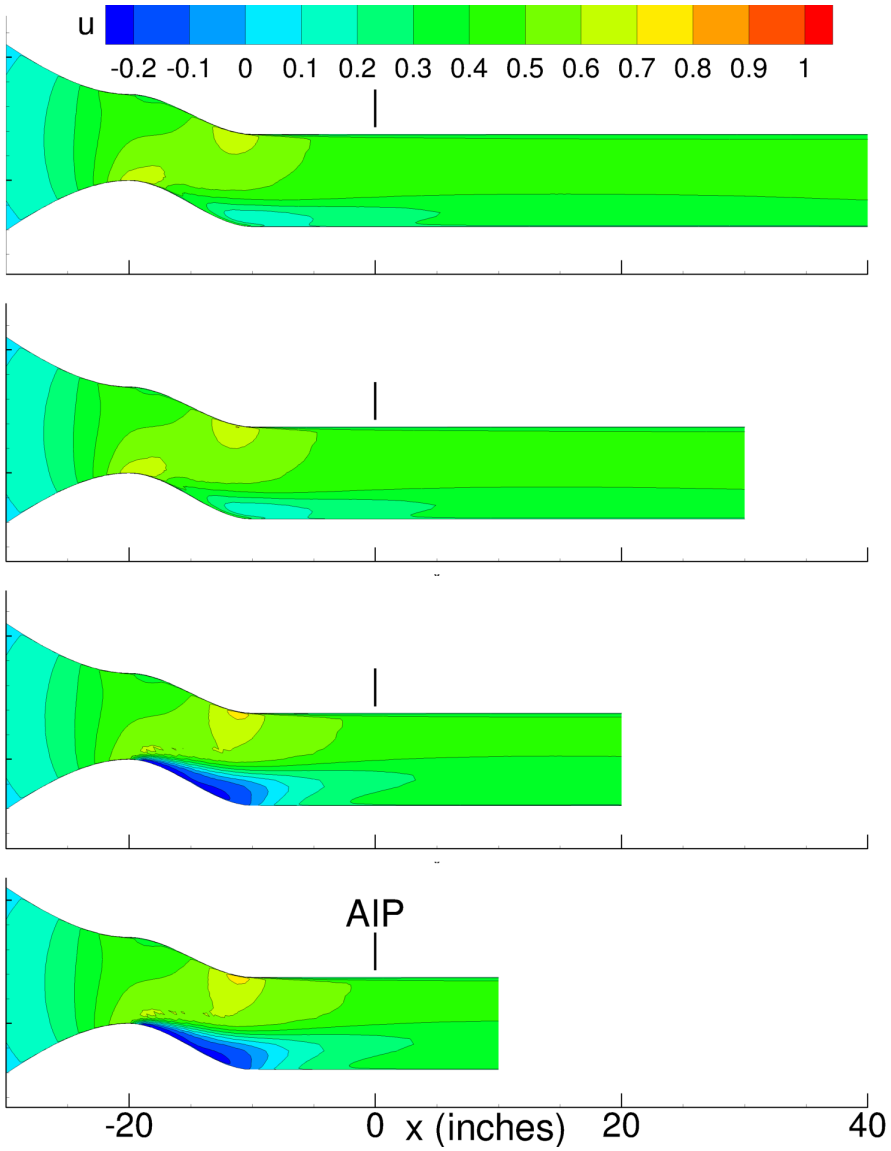

(a) Velocity contours, vertical centerplane.

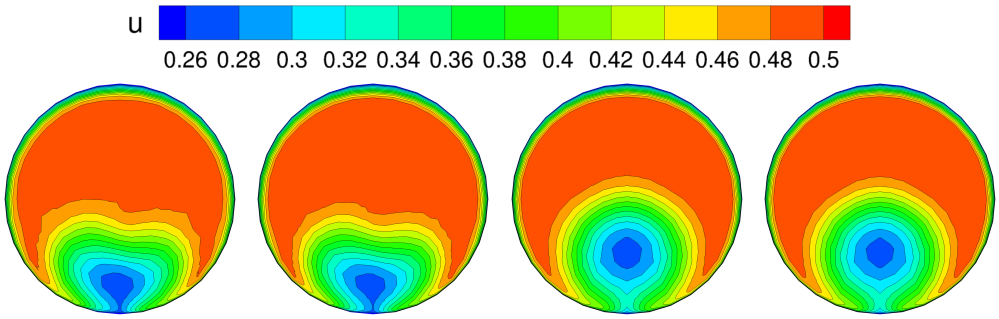

(b) AIP, $x_{exit} = 40$. (c) AIP, $x_{exit} = 30$. (d) AIP, $x_{exit} = 20$. (e) AIP, $x_{exit} = 10$.

Figure 7. Velocity contours, fixed static pressure outflow type, coarse grid, velocity non-dimensionalized by the reference speed of sound.

The changes in mass flow rate and distortion with outflow model and boundary position are plotted in Fig. 8. The mass flow rate of the choked nozzle model and the mass flow rate model match at the baseline ($x_{exit} = 40$) outflow boundary location, i.e., confirmation of the condition matching point. As observed in the previous update, the mass flow rate of the choked nozzle model gradually increased as the outflow boundary position progressed forward due to the viscous losses decreasing with the shorter downstream duct lengths. The mass flow boundary condition, as expected, maintained the same rate regardless of outflow boundary location.

Neither the AIP Mach number controller nor the fixed static pressure ratio boundary displayed monotonic behavior in mass flow rate with outflow location. A shift in the mass flow rate in the duct accompanies the change in the flow structure, i.e., separated vs. attached flow, upstream of the AIP between the two downstream outflow locations and the two upstream outflow locations. The prediction of distortion with outflow model and exit location for the 3.5-inch offset configuration is shown in Fig. 8b. Interestingly, the changes in distortion with outflow boundary location and type do not show a strong shift with the mode change in the solutions.

The same sequence of vertical centerplane and AIP velocity contour plots shown here, are discussed in the following section, Sec. 4.3, for the medium density grid solutions. Different from the coarse grid solutions, iterative convergence was not achieved at first. Initial results, modifications to the workflow, and further solution analysis are presented.

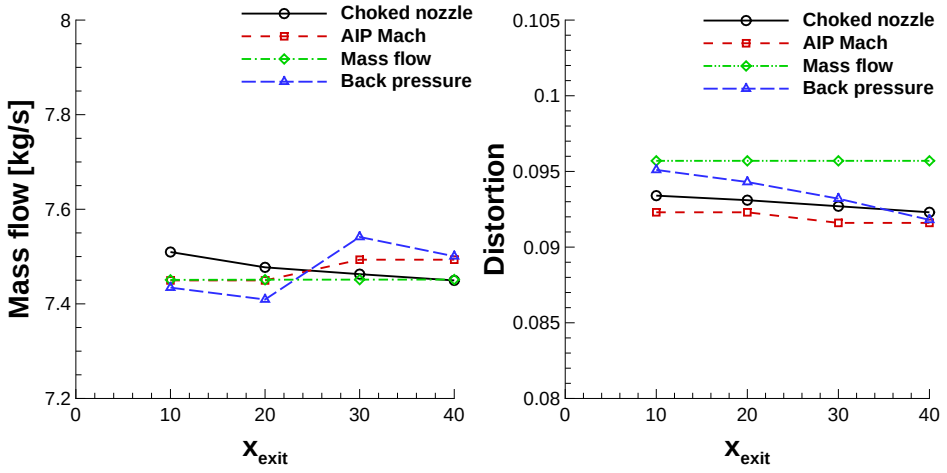

(a) Massflow.

(b) Distortion at the AIP, $(p_{t,max} - p_{t,min})/p_{t,avg}$.

Figure 8. Variation with boundary outflow model and location, baseline AIP conditions: $\dot{m} = 7.450$ kg/s, M = 0.403, SPR = 1.736, coarse grid.

4.3 Medium Grid Solutions

In this section, initial solution residuals, Sec. 4.3.1, velocity contours, Sec.4.3.2, and performance numbers, 4.3.3, are shown. The scatter in the performance data, coupled with the lack of iterative convergence, prompted studies of modifying parameters such as solution CFL and back-pressure controller strategies and are discussed in Sections 4.3.4 and 4.3.5, respectively. The final section, Sec. 4.4, explores the potential of hysteresis in inlet flow solutions that appear to be dependent on the path taken to the result.

4.3.1 Residual convergence.

The iterative convergence for the baseline, medium density grid, continuity and turbulence equations for solutions on the 3.5-inch offset duct geometry, is shown in Fig. 9. In contrast to the iterative convergence observed with the baseline, coarse density grid solutions, the residuals for all four choices for type of outflow boundary result in some kind of limit cycle or nonconvergence of the solution residual. Definitive conclusions concerning this series of solutions are elusive due to the lack of iterative convergence.

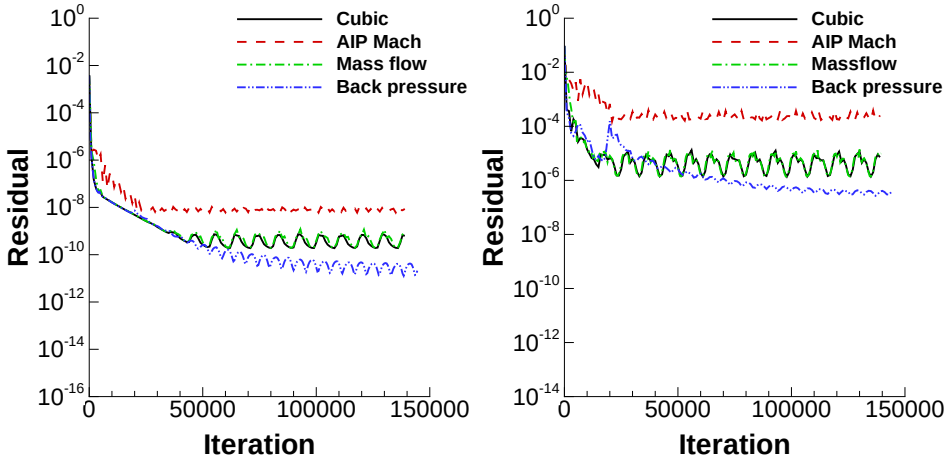

(a) Continuity equation. (b) Turbulence equation.

Figure 9. Variation of residuals with outflow boundary type, $x_{exit} = 40$.

4.3.2 Velocity contours.

Velocity contours in the vertical center-plane for the four outflow models are shown in Figs. 10-13. The streamwise velocity scales for the vertical center-plane range from -0.2 to 1.0 for the choked nozzle contour plots and -0.2 to 0.7 for the mass flow rate controller, AIP Mach controller and fixed static pressure

simulations. For increased visibility of the various flow structures, the scale for the streamwise velocity contours in the plane of the AIP was 0.0 to 0.5.

Velocity contours for the medium grid, choked nozzle outflow type solutions are shown in Fig. 10. All four outflow locations produced similar S-duct flowfields with minor variations as the outflow boundary was moved upstream closer to the AIP, as shown in Fig. 10a. Streamwise velocity contours at the AIP for each outflow boundary location are plotted in Figs. 10b-10e. The predicted streamwise velocity at the AIP shifted slightly in size and structure with variation of the the outflow boundary location. Compact, bimodal velocity contours were predicted at the AIP regardless of the location of the outflow boundary.

Velocity contours extracted from medium grid solutions developed using the AIP Mach number controller are shown in Fig. 11. This sequence of outflow boundary location simulations again displays two solution paths. Two outflow locations produced an, albeit smaller, single-mode (see Figs. 11b and 11d), while the other two produced the same compact, bimodal contours observed for the choked nozzle boundary outflow model (see Figs. 11c and 11e).

Velocity contours extracted from medium grid solutions developed using the mass flow rate controller are shown in Fig. 12. Once more, the results are somewhat inconsistent with the $x_{exit} = 30$ outflow location solution displaying the asymmetric, single-mode flowfield at the AIP.

Velocity contours extracted from medium grid solutions developed using the fixed static pressure outflow boundary are shown in Fig. 13. This sequence of outflow boundary location simulations also displays two solution paths. The streamwise velocity contours in the vertical centerplane show no reverse flow upstream of the AIP for $x_{exit} = 30$ and 40 boundary outflow locations, see Fig. 13a, while the outflow locations at $x_{exit} = 10$ and 20 again display a region of reverse flow. The streamwise velocity field in the plane of the AIP, as plotted in Figs. 13b-13e, has the same bimodal contours for outflow boundary locations of $x_{exit} = 30$ and 40, and the same larger, single-mode contours for outflow boundary locations of $x_{exit} = 10$ and 20.

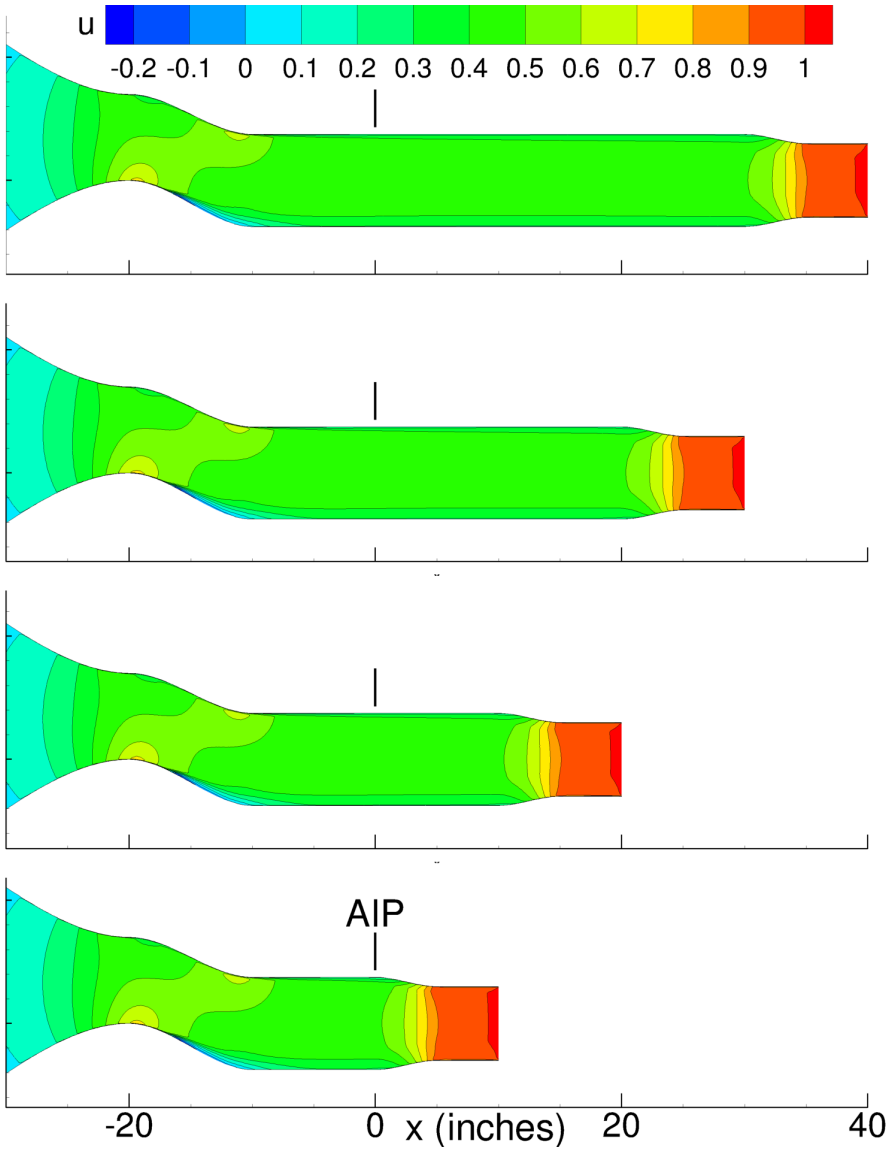

(a) Vertical centerplane.

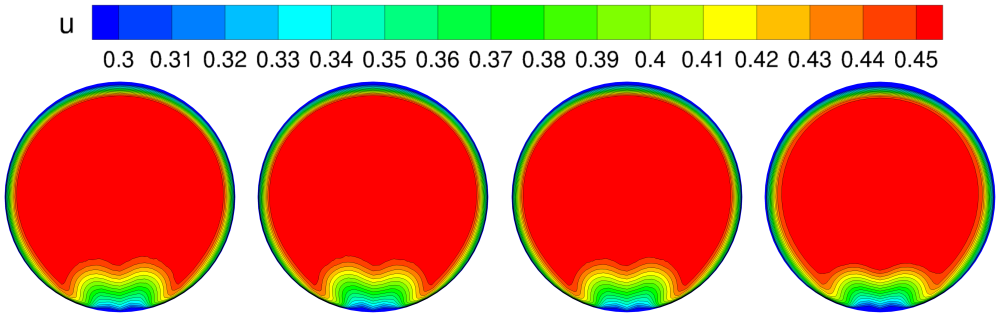

(b) AIP, $x_{exit} = 40$. (c) AIP, $x_{exit} = 30$. (d) AIP, $x_{exit} = 20$. (e) AIP, $x_{exit} = 10$.

Figure 10. Velocity contours, choked nozzle outflow type, medium grid, velocity non-dimensionalized by the reference speed of sound.

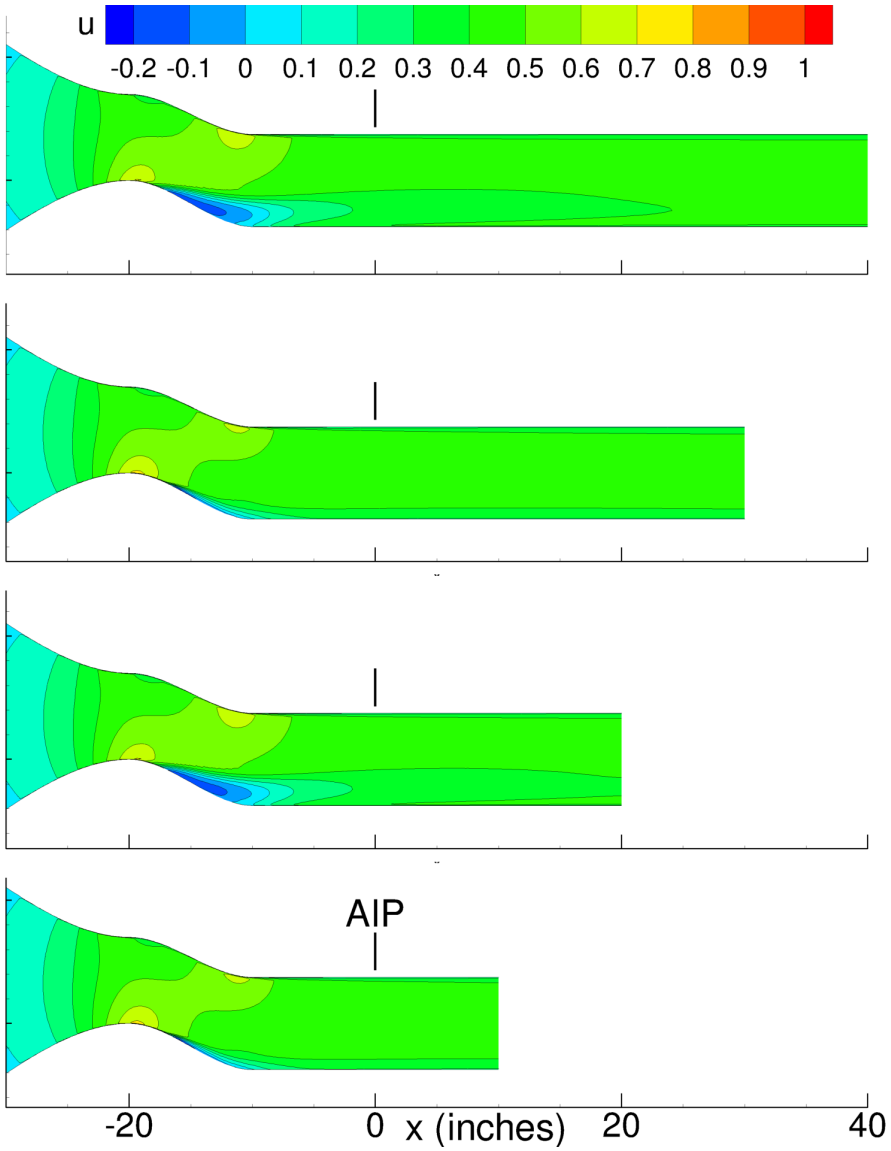

(a) Velocity contours, vertical centerplane.

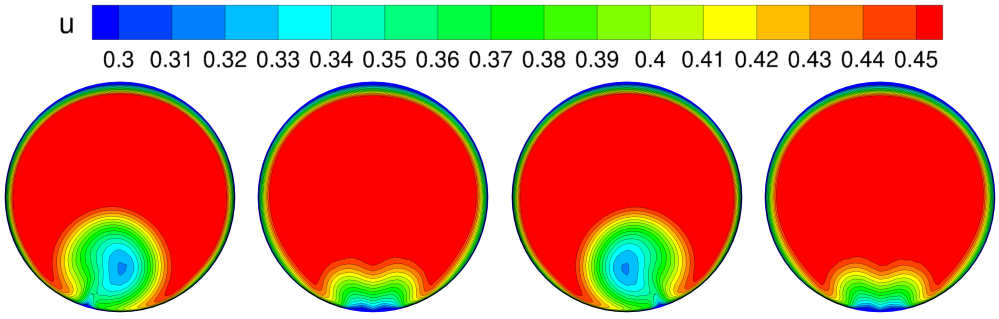

(b) AIP, $x_{exit} = 40$. (c) AIP, $x_{exit} = 30$. (d) AIP, $x_{exit} = 20$. (e) AIP, $x_{exit} = 10$.

Figure 11. Velocity contours, AIP Mach number controller outflow type, medium grid, velocity non-dimensionalized by the reference speed of sound.

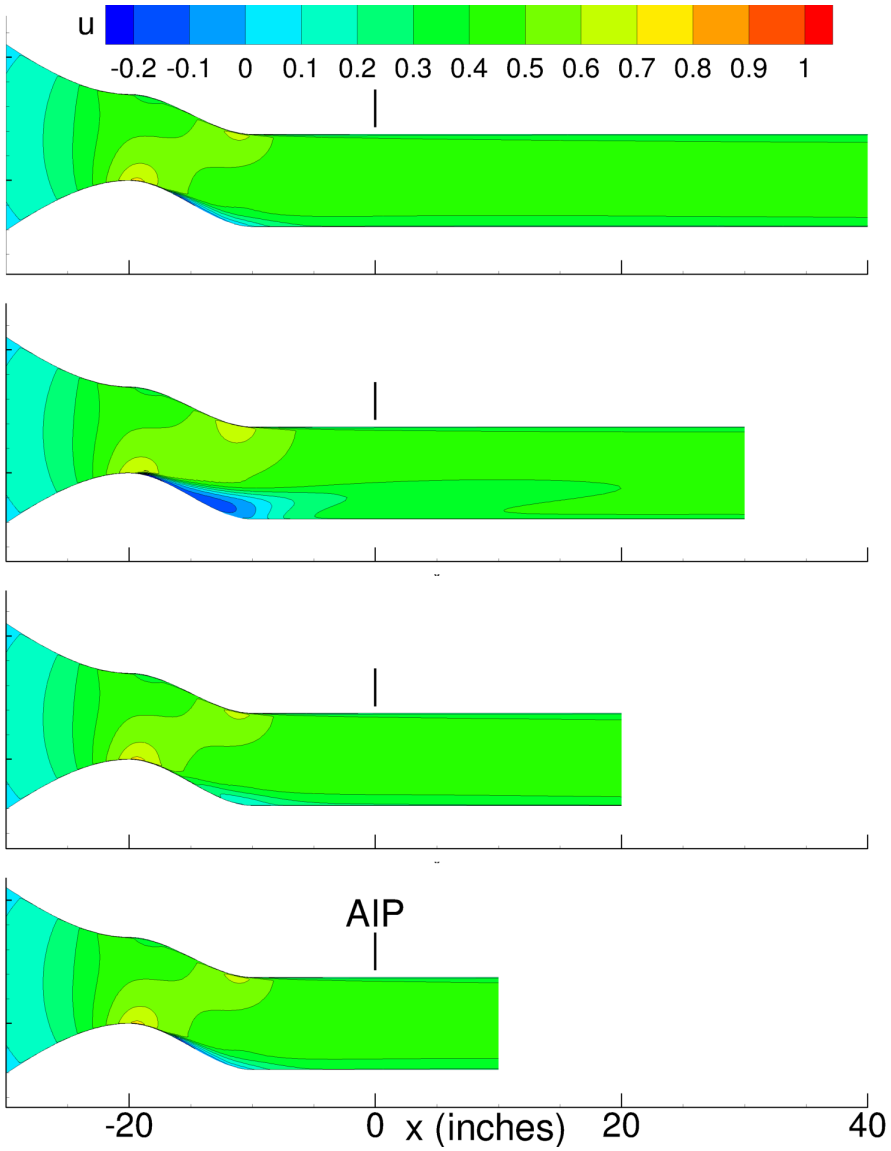

(a) Velocity contours, vertical centerplane.

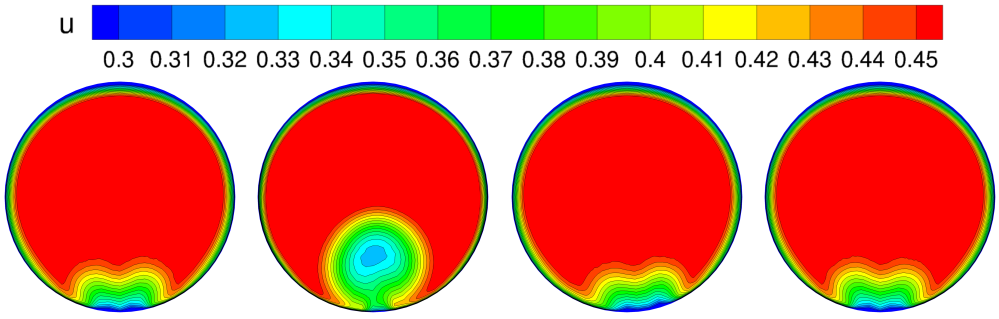

(b) AIP, $x_{exit} = 40$. (c) AIP, $x_{exit} = 30$. (d) AIP, $x_{exit} = 20$. (e) AIP, $x_{exit} = 10$.

Figure 12. Velocity contours, mass flow rate controller outflow type, medium grid, velocity non-dimensionalized by the reference speed of sound.

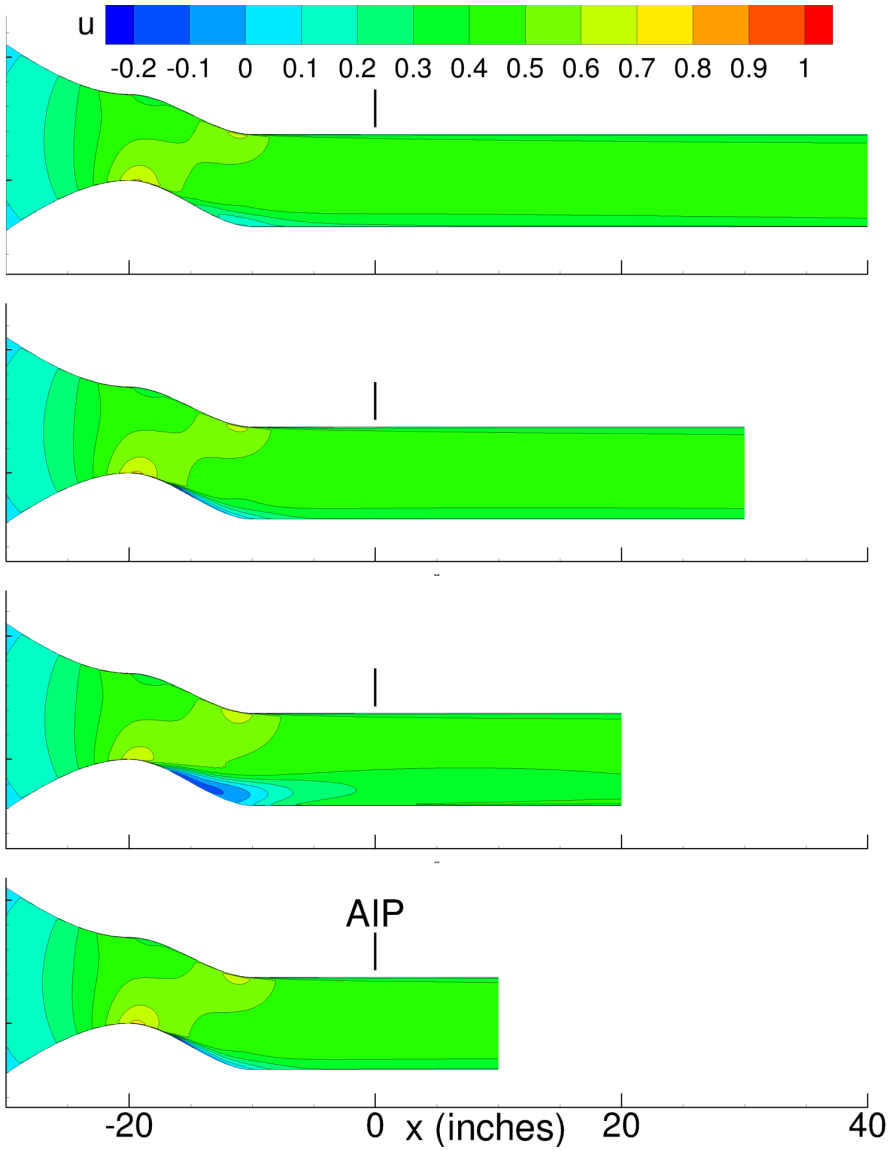

(a) Velocity contours, vertical centerplane.

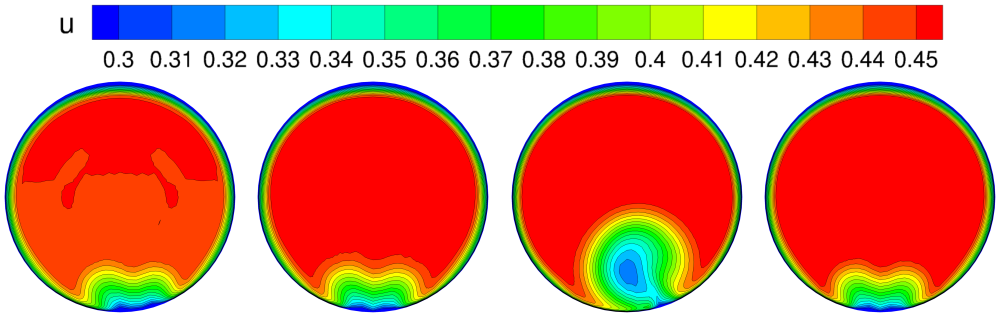

(b) AIP, $x_{exit} = 40$. (c) AIP, $x_{exit} = 30$. (d) AIP, $x_{exit} = 20$. (e) AIP, $x_{exit} = 10$.

Figure 13. Velocity contours, fixed static pressure outflow type, medium grid, velocity non-dimensionalized by the reference speed of sound.

4.3.3 Performance.

The changes with outflow model and outflow boundary position in the predicted mass flow rate and distortion for solutions developed on the medium density grid are plotted in Fig. 14. The mass flow rate of the choked nozzle model and the mass flow rate model match at the $x_{exit} = 0$ (baseline) outflow boundary location. Similar to previous results, the mass flow rate monotonically increased using the choked nozzle outflow type as the location of the outflow boundary progressed towards the location of the AIP. The choked nozzle outflow boundary was the only outflow type that developed a twin vortex structure in the S-duct at all four boundary locations, as shown in Fig. 10.

The mass flow boundary condition remained constant regardless of outflow boundary location as expected. In the case of the $x_{exit} = 30$ geometry, the controller compensated for the mode switch away from the twin vortex pair to the more expansive single vortex structure by dropping the back-pressure slightly, see Table 2. The AIP Mach controller, similarly dropped the back-pressure for the $x_{exit} = 40$ and 20 outflow locations to compensate for mode change. While the AIP Mach number controller seeks to maintain the requested average Mach number at the AIP, it does not necessarily maintain a constant mass flow rate, see Table 3.

Solutions using the fixed static pressure (back-pressure) outflow condition were quite sensitive to the location of the outflow boundary. The flow upstream of the AIP appears to progress from attached to separated as the the outflow boundary moves from $x_{exit} = 40$ to 30 to 20, reattaching with the outflow boundary at $x_{exit} = 10.$, as shown in Fig.13. Compared to the average level, the mass flow rate dropped by almost 2% relative to the outflow boundary location of 20, see the blue dashed double-dotted line in Fig. 14a.

Table 2. Variation of back-pressure (p_{back}/p_∞) with boundary condition type and location.

Boundary type	Boundary location (x_{exit})			
	40	30	20	10
Choked nozzle	1.002	1.003	1.004	1.006
AIP Mach controller	1.744	1.759	1.751	1.766
Mass flow rate	1.756	1.744	1.763	1.767
Fixed static pressure	1.763	1.763	1.763	1.763

The prediction of distortion with outflow model and exit location for the 3.5-inch offset configuration is shown in Fig. 14b. The trends of the predicted inlet distortion with outflow boundary position were quite erratic, mostly due to the solution mode switching. It is surprising to have results as consistent as

Table 3. Variation of Mach number at the AIP with boundary condition type and location.

Boundary type	Boundary location			
	40	30	20	10
Choked nozzle	0.402	0.403	0.404	0.405
AIP Mach controller	0.403	0.403	0.403	0.403
Mass flow rate	0.402	0.406	0.402	0.402
Fixed static pressure	0.396	0.399	0.393	0.406

these considering that most of the simulations were not able to attain iterative residual convergence.

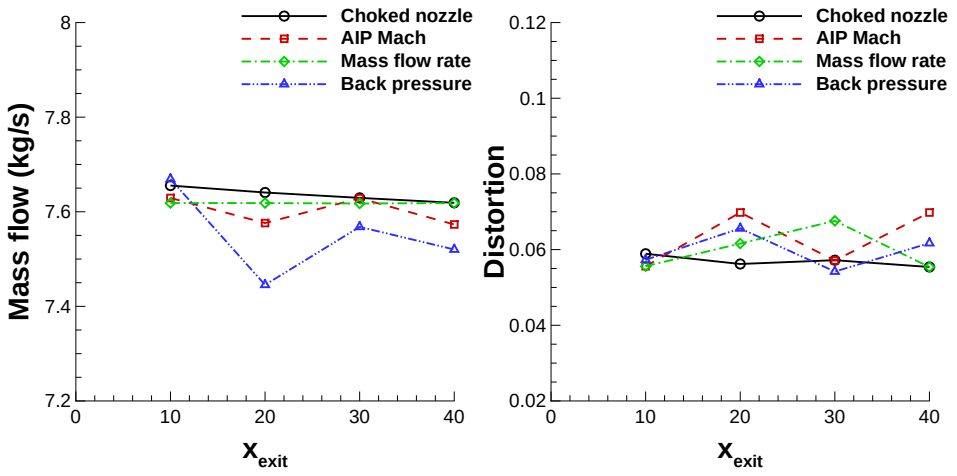

(a) Massflow.

(b) Distortion at the AIP, $(p_{t,max} - p_{t,min})/p_{t,avg}$.

Figure 14. Variation with boundary outflow model and location, baseline AIP conditions: $\dot{m} = 7.450$ kg/s, M = 0.403, SPR = 1.736, medium grid.

4.3.4 Revisit of solutions using the mass flow rate controller.

In light of the lack of iterative convergence and inlet flow mode switching issues discussed in Sec. 4.3.1, variations of CFL number and controller parameters were investigated in an attempt to improve the solution convergence. This section will briefly discuss two mass flow rate outflow boundary solutions obtained using identical boundary conditions, but slightly different mass flow rate controller parameters. The solution strategy for these simulations is typically divided into two phases: a start-up to deal with initial transients and

then a restart for solution "run out" to eventual iterative convergence. The parameters employed during these phases are usually mean and turbulence equation CFL levels, and rates of ramping up, the PID controller coefficients, and the PID controller update frequency. The original strategy employed for the baseline configuration, medium grid, is listed in Table 4. The start-up was run for 5000 iterations where the CFL for the mean and turbulent flow equations were ramped from the initial to final value over the first 1000 iterations and then held constant after that. The original tactic with the PID controller used an update frequency of 500 for the initial phase, switching to a higher frequency of every 200 iterations for the restart phase. The modified strategy cut the proportional term by a factor of 2, increased the integral term by a factor of 2 and stretched out the initial phase updates by a factor of 2.

Table 4. Simulation strategy for the baseline geometry, medium grid using mass flow rate outflow type.

Solution strategy	CFL				k_p	k_i	PID update frequency	
	Mean flow		Turbulence					
	Initial	Final	Initial	Final			Initial	Restart
Original	20	100	50	200	2×10^{-2}	1×10^{-3}	500	200
Modified	20	100	50	200	1×10^{-2}	2×10^{-3}	1000	200

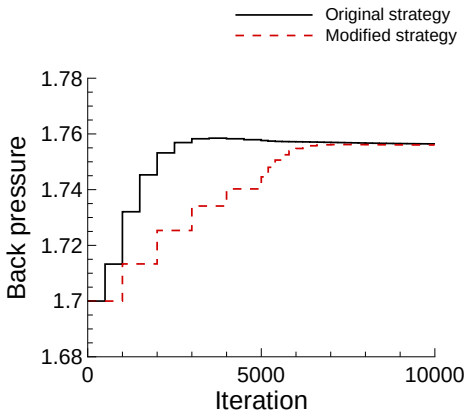

Figure 15. Comparison of back-pressure histories, mass flow rate controller, medium grid.

A comparison of the back-pressure history of the two solution strategies is plotted in Fig. 15. The solution residual histories are plotted in Fig. 16. The modified strategy slowed the timing and magnitude of the back-pressure updates. This disturbed a feedback mechanism that was destabilizing within

the original strategy causing the limit cycle observed in the solution residuals. The more stable vortex pair allowed for the solution residuals to converge another 8 orders below the level of the original strategy. Comparisons between the two approaches of the predicted mass flow and distortion are shown in Fig. 17. As expected, both solution strategies maintained the correct mass flow rate, since that was the set condition of the simulation, as shown in Fig. 17a The predicted distortion with outflow boundary location, shown in Fig. 17b, changed very little with location of the outflow boundary using the modified strategy.

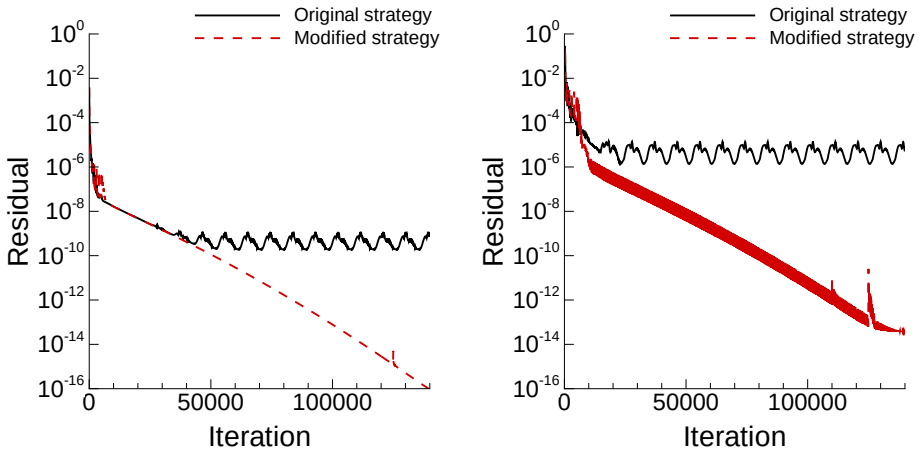

(a) Continuity equation.

(b) Turbulence equation.

Figure 16. Variation of residuals with controller strategy, $x_{exit} = 40.$, mass flow rate controller, medium grid.

Total pressure contours at the AIP and the delta between the two solutions are plotted in Fig. 18. Visual inspection of Figs. 18a and 18b show two very similar sets of contours. Contours of the difference in total pressure between the two solutions, plotted in Fig. 18c, range from $\pm$ 6 lbf/ft^2, or roughly 0.5% of the reference pressure. The total pressure difference between the two solutions in the vertical centerplane is shown in Fig. 19. Despite the improved iterative convergence achieved with the modified strategy, the resulting solutions do not appear significantly different. The difference in the streamwise velocity fields in the vertical centerplane of the two solutions was also quite small, as shown in Fig. 20.

4.3.5 Revisit of solutions using the AIP Mach number controller.

This section looks at another multiple-solution path situation, in this case, when using the recently implemented AIP Mach number controller. Again, as in the previous discussion in Sec. 4.3.4, several run-time parameters were

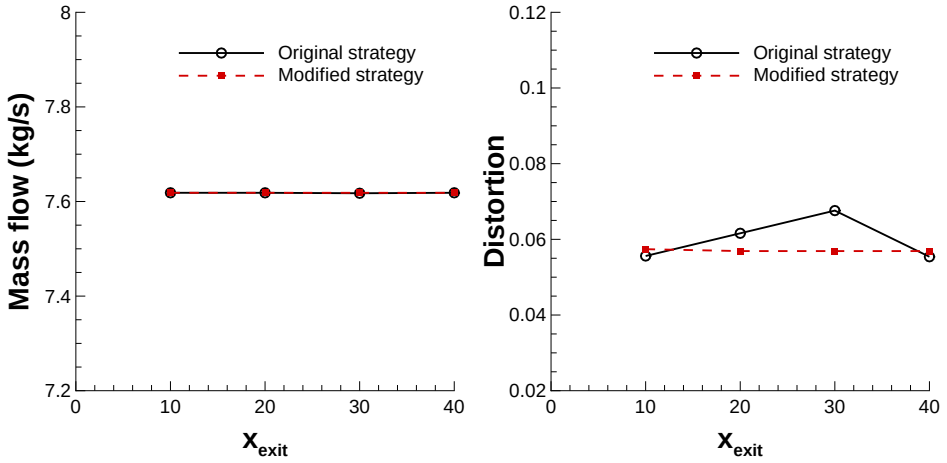

(a) Massflow.

(b) Distortion at the AIP, $\left(p_{t,max} - p_{t,min}\right)/p_{t,avg}$.

Figure 17. Comparison of strategies, variation with outflow boundary location, set massflow rate, baseline AIP conditions: $\dot{m} = 7.450$ kg/s, M = 0.403, SPR = 1.736, medium grid.

altered in an attempt to improve the solution iterative convergence history. The strategy employed for this specific simulation, which was albeit discovered by trial and error, involved reworking the CFL ramping of the mean and turbulent flow equations. In addition, the equation for the integral term was refactored for the AIP Mach controller to align with the methodology used by the mass flow rate controller. The controller coefficients and updating were left unchanged. Comparisons of the CFL schedules and the resulting back-pressure histories are shown in Fig. 21. The original CFL ramping was quite aggressive, starting from levels of 20 and 50 for the mean flow and turbulence equations, respectively, scheduled to reach the final values of 100 and 200, respectively, after the first 1000 iterations, (see the black solid lines in Fig. 21a). This particular CFL schedule was found to work quite well for many previous simulations of the choked nozzle, mass flow rate and fixed static pressure ratio configurations. The simulation in Sec. 4.3.4 used this scheduling, as listed in Table 4. The combination of a more relaxed CFL schedule, as shown by the red dashed lines in Fig. 21a, and the less aggressive controller output (due to the refactored integral equation) in the controller, comparing the black solid and red dashed lines in Fig. 21b, resulted in a solution state where the code could achieve iterative convergence, as shown in Fig. 22.

While lower CFL numbers and smaller boundary condition perturbations by the controller could be straightforward tactics for improving iterative convergence, a coherent strategy to achieve that result is not obvious.

The two solution strategies are again compared looking at the predicted

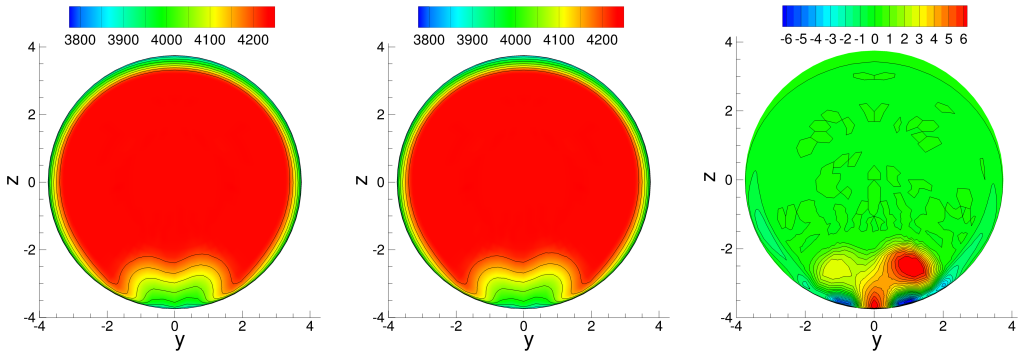

(a) Total pressure, original strategy.

(b) Total pressure, modified strategy.

(c) Difference in total pressure, $p_{t,original} - p_{t,modified}$.

Figure 18. Total pressure contours at the AIP, $x_{exit} = 40$. (baseline) geometry, mass flow rate controller, medium grid, scales in units of lbf/ft^2.

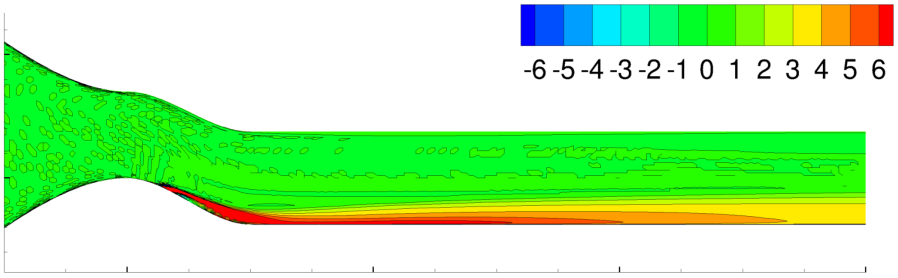

Figure 19. Difference in total pressure contours, $p_{t,original} - p_{t,modified}$, vertical centerplane, mass flow rate controller, medium grid, scale in units of lbf/ft^2.

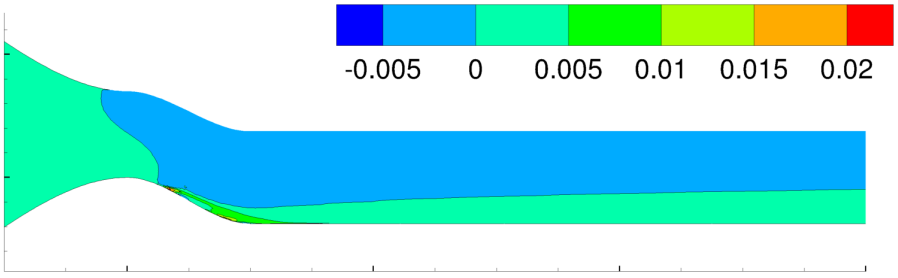

Figure 20. Difference in streamwise velocities, $u_{original} - u_{modified}$, vertical centerplane, mass flow rate controller, medium grid, velocity non-dimensionalized by the reference speed of sound.

mass flow and distortion when the back-pressure is set using the AIP Mach controller and are shown in Fig. 23. Solutions produced using the original CFL and controller parameters resulted in erratic changes in mass flow and inlet distortion with outflow boundary location, see the black solid line in

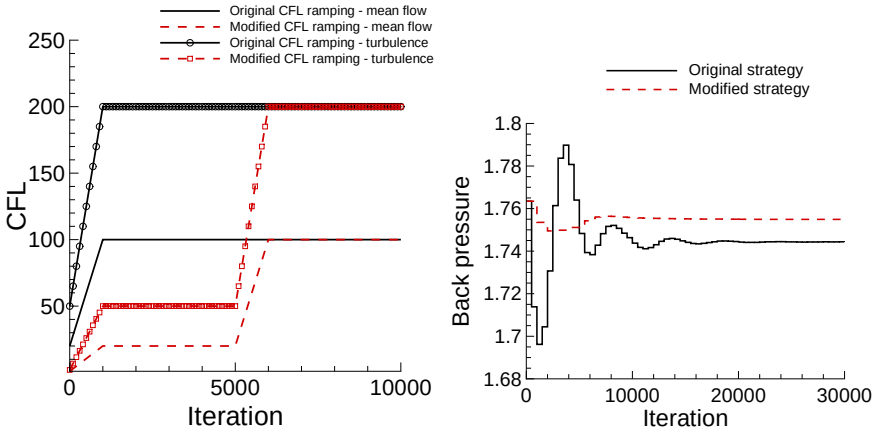

(a) CFL histories. (b) Back pressure histories.

Figure 21. Strategy difference, $x_{exit} = 40.$, AIP Mach number controller, medium grid.

Figs. 23a and 23b. The modified CFL ramping, similar to what was observed in Sec. 4.3.4, again produced more consistent results, see the red dashed line in Figs. 23a and 23b.

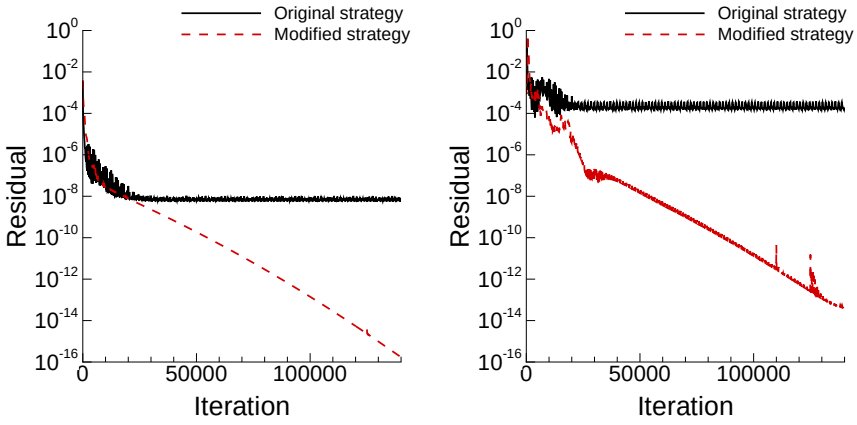

(a) Continuity equation. (b) Turbulence equation.

Figure 22. Variation of residuals with controller strategy, $x_{exit} = 40.$, AIP Mach number controller, medium grid.

Total pressure contours at the AIP and the difference between the two solutions are plotted in Fig. 24. In contrast to the two solutions using the mass flow rate outflow boundary solutions comparison, the differences between the total pressure fields at the AIP when using the AIP Mach controller was significantly larger, compare Fig. 24a to Fig. 24b. The more stable, symmetric vortex pair is observed in the solution with the modified strategy. In the ver-

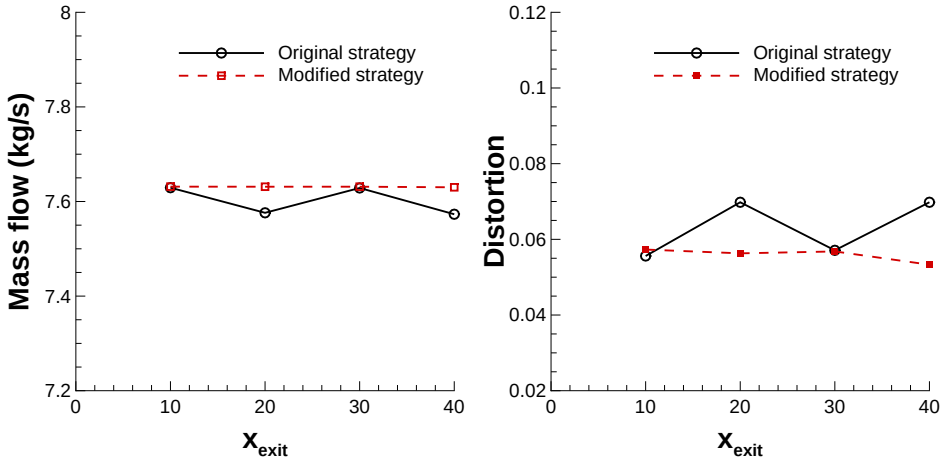

(a) Massflow.

(b) Distortion at the AIP, $\left(p_{t,max} - p_{t,min}\right)/p_{t,avg}$.

Figure 23. Comparison of strategies, variation with outflow boundary location, set Mach number at AIP, baseline AIP conditions: $\dot{m} = 7.450$ kg/s, M = 0.403, SPR = 1.736, medium grid.

tical centerplane (Fig. 25), the greatest difference in the total pressure fields spanned from the S-duct to some distance downstream of the AIP. The difference in the streamwise velocity fields were of comparable magnitude and extent, as shown in Fig. 26.

Table 5. Strategy summary results, x_{exit} = 40 (baseline) configuration, AIP Mach controller.

Solution strategy	AIP Mach	Mass flow (kg/s)	Average p_t	Distortion	p_{back}/p_∞
Original	0.403	7.573	1.406	0.0698	1.744
Modified	0.403	7.632	1.415	0.0560	1.755

Several parameters for the two simulation strategies are listed in Table 5. The requested average Mach number at the AIP of 0.403 was achieved by the back pressure controller. The difference in the mass flow rate and average total pressure between the two solution strategies was less that 1%. The predicted distortion drops down close to the level of the choked nozzle and mass flow rate boundary type solutions with this modified strategy.

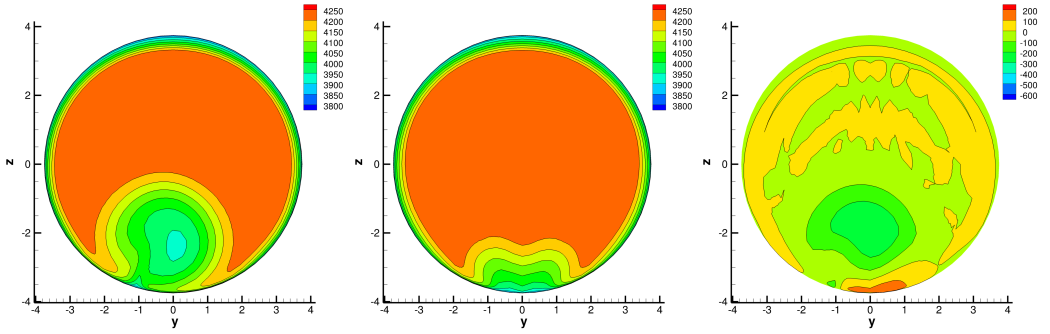

(a) Total pressure, original strategy.

(b) Total pressure, modified strategy.

(c) Difference in total pressure, $p_{t,original} - p_{t,modified}$.

Figure 24. Total pressure contours at the AIP, $x_{exit} = 40$. (baseline) geometry, AIP Mach number controller, medium grid, scales in units of lbf/ft^2.

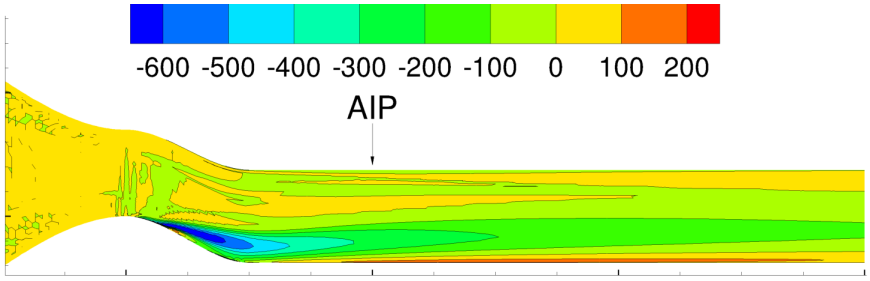

Figure 25. Difference in total pressure, $p_{t,original} - p_{t,modified}$, vertical centerplane, AIP Mach number controller, medium grid, scale in units of lbf/ft^2.

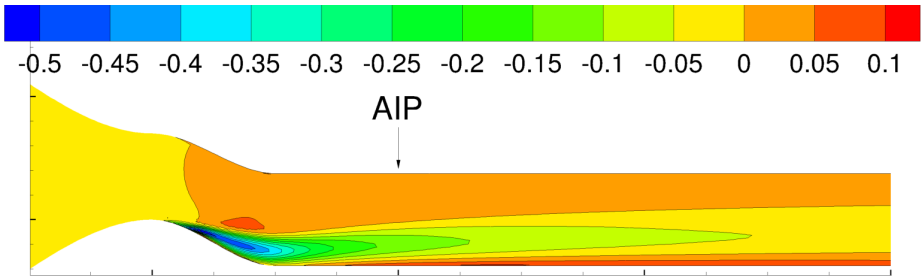

Figure 26. Difference in streamwise velocities, $u_{original} - u_{modified}$, vertical centerplane, AIP Mach number controller, medium grid, velocity nondimensionalized by the reference speed of sound.

4.4 Solution hysteresis study.

This section looks at the effect of progressing from one fixed point static pressure ratio setting to another restarting from a previously established solution.

Two fixed point solutions were first run from scratch: one using a low pressure ratio, p_{back}/p_∞ = 1.55, and the other a high pressure, p_{back}/p_∞ = 1.95. The first set of runs sequenced through every $\delta p/p_\infty$ = 0.05 starting at p_{back}/p_∞ = 1.55 stopping at p_{back}/p_∞ = 1.95. The second set started at p_{back}/p_∞ = 1.95 and sequenced through the same $\delta p/p_\infty$ = 0.05 increments stopping when p_{back}/p_∞ = 1.55. Several intermediate fixed point static pressure ratio simulations were run from scratch for solution path comparisons.

The variation of predicted distortion at the AIP with increasing and decreasing fixed point static pressure ratio sweeps for the coarse and medium baseline grids are plotted in Fig. 27. The black line with circle symbol is the decreasing pressure ratio sweep and the red dashed line with squares is the increasing pressure ratio sweep. The coarse grid solutions, shown in Fig. 27a, for the decreasing pressure ratio sweep, display a distinct change in solution mode between 1.7 and 1.8. The increasing pressure ratio curve does not show any obvious deviation in the rate of change of the distortion with static pressure applied at the outflow boundary.

The same static pressure sweep performed using the medium density grid, as shown in Fig. 27b, displayed some hysteresis, but not to the degree observed with the coarse grid solutions. The distortion numbers extracted from a number of fixed point solutions, plotted as green diamonds in Fig. 27b, flip back and forth between the black increasing static pressure sweep line and the red decreasing static pressure sweep line. The predicted distortion for the pressure sweeps are fairly coincident at the end points, but diverge where the development of the vortex structures and separation are sensitive to the solution history.

The same increasing and decreasing static pressure sweeps were performed on the series of outflow boundary locations and are plotted in Fig. 28. For clarity, all the decreasing sweeps are shown in one plot, Fig. 28a, and all of the increasing pressure sweeps are shown in Fig. 28b. The trend of the four outflow boundary locations were closely grouped at the high pressure ratios. At pressure ratio level less than 1.75, each configuration took a slightly different path. For the increasing pressure ratio sweep, Fig. 28b, the predicted distortion levels of the four outflow location configurations tracked closely throughout the whole range. The flow structure established with the p_{back}/p_∞ = 1.55 fixed point solution seems to persist preventing any mode switching from occurring.

In Balin [16], the issue of multiple solutions was discussed in the context of the lift-curve with the high-lift Common Research Model (HL-CRM). Balin discusses the dependence on start-up transients and initial conditions as to which solution branch was taken by code. Balin also investigated what improvements might be found with using eddy-resolving methods such as DDES [17]. That may be an option to investigate in the next phase of the inlet boundary condition study.

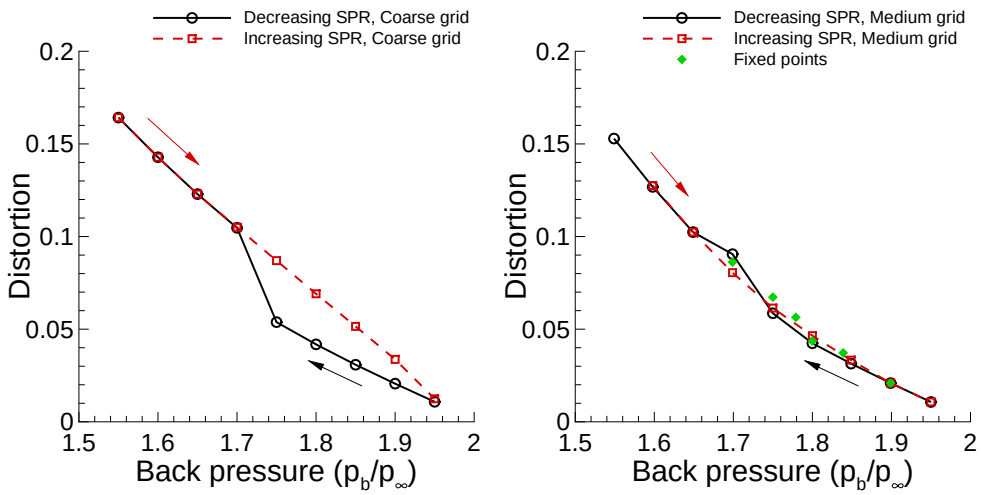

(a) Coarse grid. (b) Medium grid.

Figure 27. Change in predicted inlet distortion with static pressure ratio, restart sweeps, x_{exit} (baseline) configuration.

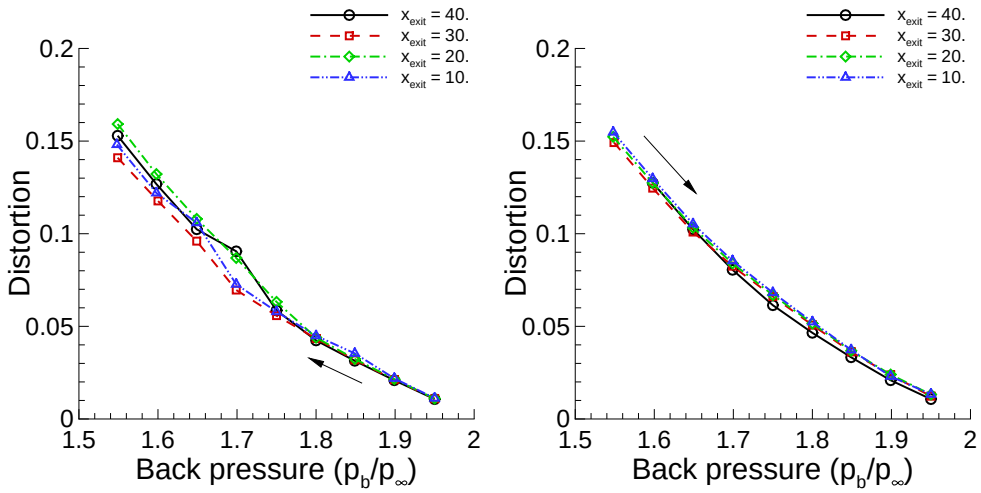

(a) Decreasing static pressure ratio sweep. (b) Increasing static pressure ratio sweep.

Figure 28. Change in predicted inlet distortion with static pressure ratio, restart sweeps, outflow boundary location variation.

5 Summary

The effect on inlet mass flow rate and distortion with variations in the outflow boundary condition streamwise location and physical modeling models were studied. The outflow physical models included a choked nozzle, outflow Mach number, mass flow rate, and static pressure boundary conditions. Additionally, results using the average Mach number at the AIP to drive the back-pressure was discussed. The choked flow nozzle was the most consistent outflow boundary model for changes in distortion with outflow boundary location, followed by the mass flow rate controller outflow boundary model. Placing the outflow boundary downstream and not coincident with the AIP is recommended.

Mode-switching between asymmetric single vortex and symmetric vortex pair solutions occurred for the mass flow rate controller, AIP Mach number controller, and the fixed static pressure outflow boundary models as the outflow boundary location moved closer to the AIP. Start-up transients and initial conditions appear to influence which solution path was taken. Hysteresis was observed with fixed static pressure solution restarts of decreasing pressure ratio at the outflow boundary (initially a low Mach number at the AIP) compared to restarting from a low pressure ratio increasing to higher levels (initially a high Mach number at the AIP).

Acknowledgments

This work was supported by the NASA Civilian Supersonic Transport project. Makoto Endo of the Engine Combustion Branch at the Glenn Research Center is acknowledged for the initial implementation of using the Mach number calculated from a control surface at the AIP to drive the back-pressure PID controller. Considerable appreciation is extended to NASA-Langley's Mid-range Computing K-cluster management and system administrators for providing an extremely productive computing environment for performance of this body of work.

6 Nomenclature

Roman letters

a	speed of sound
k_p, k_i, k_d	PID-controller constants
$\dot{m}$	mass flow, (kg/s)
M	Mach number
p	pressure
Re	Reynolds number

T	temperature
u	Streamwise Cartesian velocity
x,y,z	Cartesian directions
p_{back}	back-pressure, p/p_∞

Subscripts

back	back-pressure
exit	at location of exit boundary
t	total conditions
∞	freestream condition

Conventions

AIP	aerodynamic interface plane
CFD	computational fluid dynamics
CFL	Courant-Friedrichs-Lewy
PID	Proportional-Integral-Derivative
QCR	quadratic constitutive relation
RANS	Reynolds averaged Navier-Stokes
RC	rotation correction
SA	Spalart-Allmaras
SPR	static pressure ratio

References

1. Roe, P. L.: Approximate Riemann Solvers, Parameter Vectors, and Difference Schemes. *J. Comp. Phys.*, vol. 43, 1981, pp. 357–372.

2. van Leer, B.: Towards the Ultimate Conservative Difference Schemes V. A second order sequel to Godunov's Method. *J. Comp. Phys.*, vol. 32, 1979, pp. 101–136.

3. Biedron, R. T.; Carlson, J.-R.; Derlaga, J. M.; Gnoffo, P. A.; Hammond, D. P.; Jones, W. T.; Kleb, W.; Lee-Rausch, E. M.; Nielsen, E. J.; and Park, M. A.: FUN3D Manual: 13.2. NASA TM–2017-219661, Aug. 2017.

4. `https://fun3d.larc.nasa.gov`. Accessed: 2017-03-20.

5. Spalart, P. R.; and Allmaras, S. R.: A One-Equation Turbulence Model for Aerodynamic Flows. *Recherche Aerospatiale*, vol. 1, 1994, pp. 5–21.

6. M. L. Shur, M. K. Strelets, A. K. T.; and Spalart, P. R.: Turbulence Modeling in Rotating and Curved Channels: Assessing the Spalart-Shur Correction. *AIAA Journal*, vol. 38, no. 5, 2000, pp. 784–792.

7. Spalart, P. R.: Strategies for Turbulence Modelling and Simulation. *International Journal of Heat and Fluid Flow*, vol. 21, 2000, pp. 252–263.

8. Jirasek, A.: Mass Flow Boundary Conditions for Subsonic Inflow and Outflow Boundary. *AIAA Journal*, vol. 44, no. 5, 2006, pp. 939–947.

9. Krist, S. L.; Biedron, R. T.; and Rumsey, C. L.: CFL3D User's Manual (Version 5.0). NASA TM–1998-208444, June 1998.

10. Carlson, J.: Inflow/Outflow Boundary Conditions with Application to FUN3D. NASA TM–2011-217181, October 2011.

11. Advisory Group for Aerospace Research and Development: Sonic Nozzles for Mass Flow Measurement and Reference Nozzles for Thrust Verification. NATO Research and Technology Organisation AGARD AR-321, June 1997.

12. Carlson, J.-R.: Automated Boundary Conditions for Wind Tunnel Simulations. NASA TM–2018-219812, Mar. 2018.

13. Carter, M. B.; Bozeman, M. D.; and Carlson, J.-R.: USM3D and FUN3D Results for S-duct Configuration. , July 2018.

14. Endo, M.: Private Communication, 2020. Improvements to the back pressure controller he implemented using Mach number calculated at the AIP.

15. Nishikawa, H.; Diskin, B.; Thomas, J.; and Hammond, D.: Recent Advances in Agglomerated Multigrid. 01 2013.

16. Balin, R.; and Jansen, K. E.: A Comparison of RANS, URANS, and DDES for High Lift Systems from HiLiftPW-3. AIAA Paper 2018-1254, 2018.

17. Spalart, P. R.; Deck, S.; Shur, M. L.; Squires, K. D.; Strelets, M. K.; and Travin, A.: A New Version of Detached-eddy Simulation, Resistant to Ambiguous Grid Densities. *Theoretical and Computational Fluid Dynamics*, vol. 20, no. 3, July 2006, pp. 181–195.

REPORT DOCUMENTATION PAGE

Form Approved
OMB No. 0704–0188

1. REPORT DATE *(DD-MM-YYYY)*	2. REPORT TYPE	3. DATES COVERED *(From - To)*
01-03-2022	Technical Memorandum	

4. TITLE AND SUBTITLE
Identification of Best Practices for Predicting Inlet Performance Using FUN3D Part 1: Isolated S-Duct.

5a. CONTRACT NUMBER

5b. GRANT NUMBER

5c. PROGRAM ELEMENT NUMBER

6. AUTHOR(S)
Carlson, Jan-Reneé; Bozeman, Michael D., Jr.

5d. PROJECT NUMBER

5e. TASK NUMBER

5f. WORK UNIT NUMBER
109492.02.07.01.01.01

7. PERFORMING ORGANIZATION NAME(S) AND ADDRESS(ES)
NASA Langley Research Center
Hampton, Virginia 23681-2199

8. PERFORMING ORGANIZATION REPORT NUMBER

9. SPONSORING/MONITORING AGENCY NAME(S) AND ADDRESS(ES)
National Aeronautics and Space Administration
Washington, DC 20546-0001

10. SPONSOR/MONITOR'S ACRONYM(S)
NASA

11. SPONSOR/MONITOR'S REPORT NUMBER(S)
NASA/TM–20210022123

12. DISTRIBUTION/AVAILABILITY STATEMENT
Unclassified-Unlimited
Subject Category 01
Availability: NASA STI Program (757) 864-9658

13. SUPPLEMENTARY NOTES
An electronic version can be found at http://ntrs.nasa.gov.

14. ABSTRACT

Variations in numerical model and location of the outflow boundary of a generic S-duct inlet test configuration were investigated. Outflow models were a choked convergent nozzle, back pressure using the averaged Mach number at the aerodynamic interface plane (AIP), mass flow rate, and fixed static pressure, placed at several streamwise locations downstream of the AIP. Iterative convergence was important to predict the symmetric vortex pair passing through the AIP. Distortion and mass flow rate varied slightly depending on model. A hysteresis in the predicted inlet distortion levels was observed with static pressure outflow boundary value sweeps. Moving the outflow boundary location closer to the AIP varied the shape and degree of hysteresis with no discernible consistent trend.

15. SUBJECT TERMS
FUN3D; Aerodynamics; Computational fluid dynamics; Fluid Mechanics; Mathematics; Aircraft inlets; Proportional-Integral-Derivative; Boundary conditions; Internal flow

16. SECURITY CLASSIFICATION OF:			17. LIMITATION OF ABSTRACT	18. NUMBER OF PAGES	19a. NAME OF RESPONSIBLE PERSON
a. REPORT	b. ABSTRACT	c. THIS PAGE			STI Information Desk (help@sti.nasa.gov)
U	U	U	UU	37	19b. TELEPHONE NUMBER *(Include area code)* (757) 864-9658